Supporting information to:
The optical nanosizer – quantitative size and shape analysis of individual nanoparticles by high-throughput widefield extinction microscopy

Lukas M Payne,[1,2] Wiebke Albrecht,[3,4] Wolfgang Langbein,[2,*] and Paola Borri[1]
[1] *Cardiff University, School of Biosciences, Museum Avenue, Cardiff CF10 3AX, UK*
[2] *Cardiff University, School of Physics and Astronomy, The Parade, Cardiff CF24 3AA, UK*
[3] *EMAT, University of Antwerp, Groenenborgerlaan 171, B-2020 Antwerp, Belgium*
[4] *NANOlab Center of Excellence, University of Antwerp, Belgium*
(Dated: June 18, 2020)

S.I. LED ILLUMINATION SPECTRA

The spectral intensity of the led source used in the experiment (Thorlabs LED4D106 with a set of independent LEDs of center wavelengths 405 nm, 455 nm, 530 nm, 660 nm, coupled via a liquid light guide Thorlabs AD5LLG), are given in Fig. S1, measured with an Ocean Optics USB-2000 FLG spectrometer.

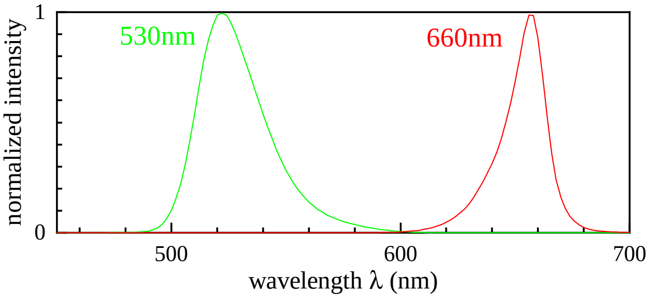

Figure S1. Plot of the two utilized LED spectra in the illumination. The green, and red curves correspond to the spectra of the 530 nm and 660 nm LEDs, respectively.

S.II. DETAILS OF PARTICLE ORIENTATION AND GEOMETRY FITTING

A. Calculation of $\sigma_{\mathrm{abs},\Lambda}$ and $\sigma_{\mathrm{sca},\Lambda}$ matrices

We begin by tabulating the depolarization factors, L_j, calculated using Eq. 3, for a set of aspect ratios, $b/a \in [\iota_1, \iota_2]$, and $c/a \in [\iota_1, \iota_2]$, with $\iota_1 > 0$ and $\iota_2 \leq 2.5$ being the lower and upper bounds of the aspect ratio ranges, respectively, used in our analysis. The grid of b/a, and c/a is taken to have a constant step size s_ι in their inverse, and a number of steps, n_ι, where $s_\iota = (1/\iota_1 - 1/\iota_2)/(n_\iota - 1)$, so that $(x/a)_i = 1/(1/\iota_2 + (i-1)s_\iota)$, where x can be either b or c, and $i = 0 \ldots n_\iota$. We use the inverse to sample the LSPR shift more homogeneously.

With L_j tabulated, we create, for each channel Λ, a table of $\sigma_{\mathrm{abs},\Lambda}/V$ and $\sigma_{\mathrm{sca},\Lambda}/V^2$ over a 5D parameter space with dimensions b/a, c/a, ψ, θ, and ϕ, with $\psi \in [0, \pi]$, $\theta \in [-\pi/2, \pi/2]$, $\phi \in [0, \pi]$. To reduce the number of points we calculate, we have removed some rotational redundancies. While the unique ψ and ϕ ranges for a general object are $[0, 2\pi]$, we can instead use only half this range due to the inversion symmetry and the three reflection planes of the considered ellipsoid, leading to a periodicity of the cross-sections in ψ and ϕ with a period of π. Furthermore, because the in-plane rotation R_ψ is the first rotation from the measurement frame to the NP frame, the cross-sections are a function of $\psi - \gamma_{\mathrm{P}}$ only, such that the dependence on γ_{P} does not require an additional table dimension. For all three angles, typical step sizes used were $(\delta\phi, \delta\theta, \delta\psi) = \pi/12$. Typical grids used had on the order of 10^6 points and were computed in a few minutes on a modern CPU (AMD Ryzen Threadripper 2950X).

B. Interpolation of $\sigma_{\mathrm{abs},\Lambda}$ and $\sigma_{\mathrm{sca},\Lambda}$ matrices

We chose to perform the interpolation of the $\sigma_{\mathrm{abs},\Lambda}$ and $\sigma_{\mathrm{sca},\Lambda}$ matrices using the “griddedInterpolant” function in Matlab, which allows interpolation over n-dimensional matrices. We selected the “makima” method of interpolation, Matlab’s modified implementation of the Akima piecewise cubic Hermite interpolation [S1]. Other relevant available methods were “pchip” (piecewise cubic Hermite interpolating polynomial), and cubic “spline”. In Matlab, the “pchip” method requires that coefficients be chosen, such that the first derivative is continuous, and that the

---

* langbeinww@cardiff.ac.uk

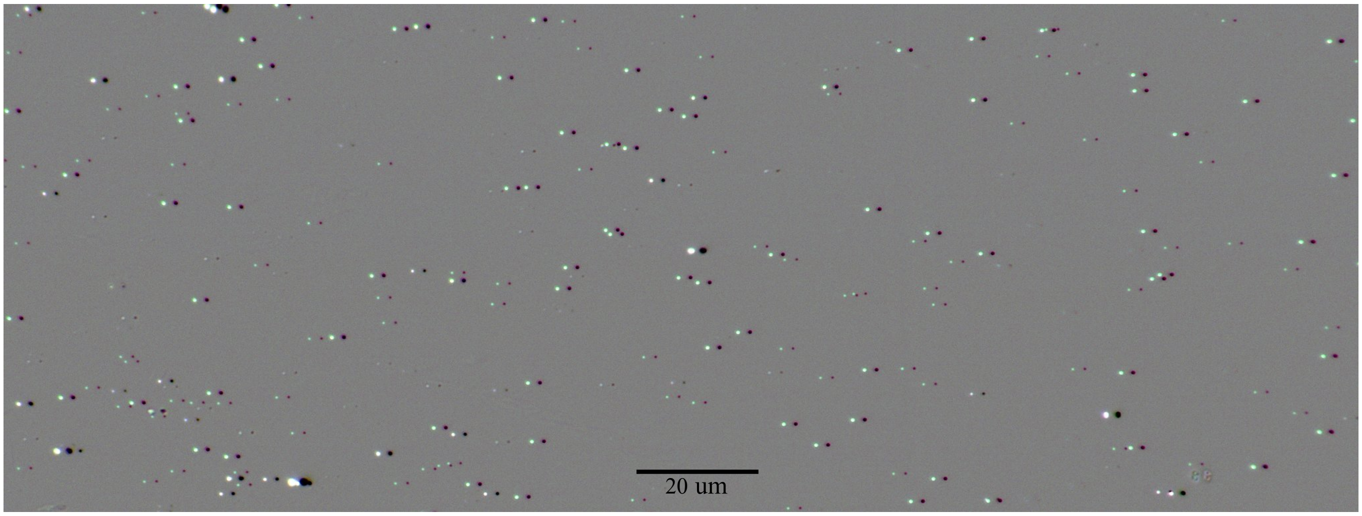

Figure S2. Full field of view (2044 × 765 pixels) of Δ_+ for $\gamma = 0^\circ$ shown cropped in Fig. 4b. Triple colour channel overlay $\Lambda = (450, 550, 600)$. The colour channel range is ±0.8%. The strong contrast features are ultra-uniform gold spheres of 50 nm diameter, which have not been analysed in the present work since the dipole approximation is unsuited for this size, as shown in Fig. S8.

interpolation exhibits local monotonicity on every interval to preserve data shape [S2]. On the other hand, Matlab's implementation of the "spline" method not only requires coefficients ensuring continuity of the second derivative, but also that there are no jumps in the third derivative at the first and last interior datapoints [S2]. This latter condition is known as the not-a-knot end condition. The "makima" method exhibits less drastic flattening, in comparison to the "pchip", while also avoiding the overshoot/ringing associated with the requirements of the "spline" method. For computational speed, the interpolation coefficients are calculated once initially, and then used in the gradient decent minimization.

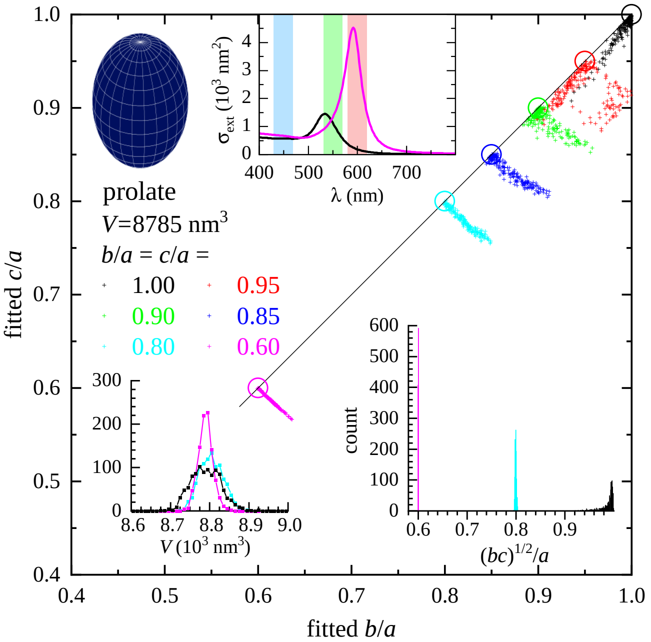

Figure S3. As Fig. 6, but assuming field averaging using condenser NA=1.34 and objective NA=1.45 conditions, and for $\hat{\sigma}_{\rm ext} = (5.11, 7.79, 4.63)\mathrm{nm}^2$.

C. NP geometry determined by fits - Simulation

Here we expand upon the discussion in Sec. 4.2, reexamining the case of fitting prolate NPs, but with hypothetically improved experimental parameters, and introducing a similar examination of oblate and ellipsoidal NPs.

We can study the effect of decreasing the experimental noise by hypothetically increasing experimental parameters, $N_{\rm r}$, NA, M, and assuming that Λ are the same as in the experiment for the UGNSs. We could make estimates of the shot-noise limited measurement noise for different experimental parameters, but from previous experiments we have observed that using a NA = 1.45 objective with total magnification, $M = 150$, and $N_{\rm r} = (16, 16, 46)$ leads to a measured noise $\hat{\sigma}_{\rm ext} = (5.11, 7.79, 4.63)\,\mathrm{nm}^2$ for $\Lambda = (450, 550, 600)$, i.e. about an order of magnitude lower than that in the presented experiment. The resulting fitted parameters for prolate NPs are given in Fig. S3. Comparing with those of Fig. 6, the precision of the parameters is improved by approximately an order of

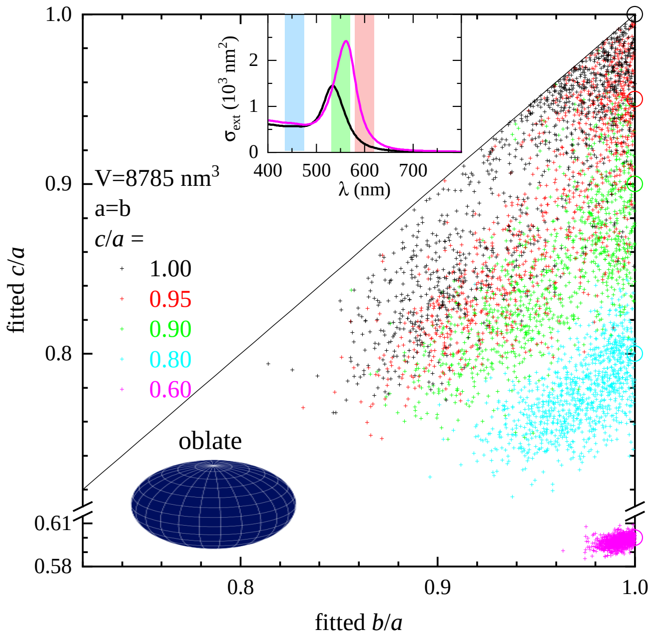

Figure S4. As Fig. 6, but for an oblate NP with a constant volume of $V = 8785\,\text{nm}^3$, $a = b$ and for various c/a as indicated.

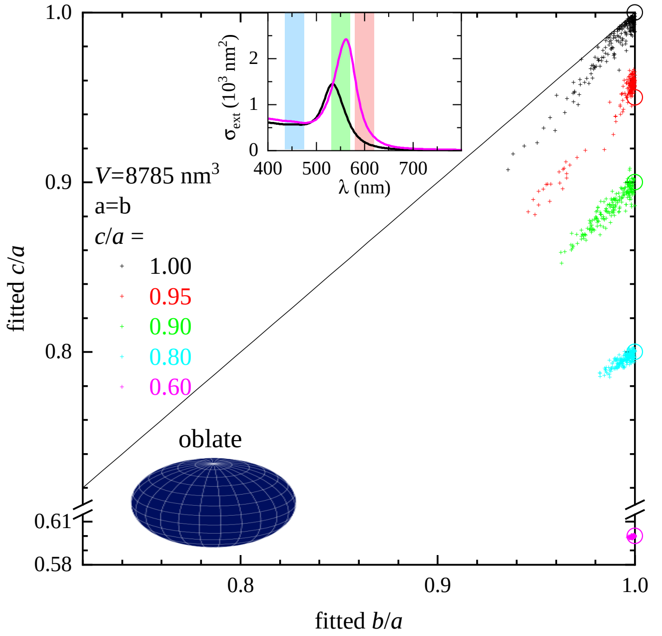

Figure S5. As Fig. S4, but assuming field averaging using condenser NA=1.34 and objective NA=1.45 conditions, and for $\hat{\sigma}_{\text{ext}} = (5.11, 7.79, 4.63)\text{nm}^2$.

magnitude in the volume. For the aspect ratios, the situation is more complicated, with the combination $\sqrt{bc}/a$ and b/c behaving differently. For a significant ellipticity, $\sqrt{bc}/a \lesssim 0.9$, the precision in $\sqrt{bc}/a$ improved also by an order of magnitude. However, the precision of b/c improves by only half an order of magnitude, indicating a quadratic dependence of the error S on variation of b/c minimized over the NP orientation. For a nearly spherical NP instead, $\sqrt{bc}/a \gtrsim 0.95$, the precision in b/c is better than in $\sqrt{bc}/a$. Clearly, the interplay between NP orientation and aspect ratios influences the measured cross-section in an intricate way.

In the oblate case shown in Fig. S4, the chosen orientation leaves a and b in-plane, so that $\sigma_{\text{ext}}(\gamma_{\text{P}})$ is independent of γ_{P} and the aspect ratio cannot be seen by the polarization dependence. The remaining effect of the aspect ratio is the red-shift in the resonance, as seen in Fig. 2b, which is, however, less pronounced than in the prolate case Fig. 2a.

Interestingly, the fitted b/a and c/a both show a low error for a simulated $c/a = 0.6$, different from the prolate case. Achieving no-polarization dependence in-plane for both colour channels, which are differently sensitive to the two LSPR frequencies, apparently constrains the fitted NP orientation to provide a fitted $a/b \approx 1$. If we compare Fig. S4 & S5, we can see the precision of the parameters is improved by half an order of magnitude in both aspect ratios, depending on the level of asymmetry.

The results for an elliptical NP of constant volume, $V = 8785\,\text{nm}^3$, with three different semi-axes (a, $b = 2a/3$, and $c = a/3$), are given in Fig. S6 for different orientations. The NP has three LSPRs, as also seen in Fig. 2 on the right, around 500, 550, and 650 nm, which are also visible in the spectra shown in Fig. S6. The weight of them in the measured extinction depends on the NP orientation. It is clearly seen that the distribution of retrieved aspect ratios depends on the simulated orientation of the NP. One can note a small set of outliers (below 1%), which arise from a different NP orientation providing similar measured data, which can be realized within the noise. We note that these outliers are not evident in the fit error S or the fitted volume V (see inset in Fig. S6 for $\theta = \phi = 0$).

To show the effect of probing the NP with intuitively more appropriate filter ranges, the simulations performed in Fig. S6 are replicated in Fig. S7 with the center wavelength of the red channel shifted to 650 nm. Better aligning the filter spectral range to the position of the red-shifted NP resonance, results in the distributions resembling more closely those in Fig. 6 with the dispersion of the results forming arcs about $b/a = c/a = 1$, while the distribution is centered at the expected values b/a and c/a. Surprisingly, the new choice of spectral range, even though better fitting to the LSPRs, does not lead to a

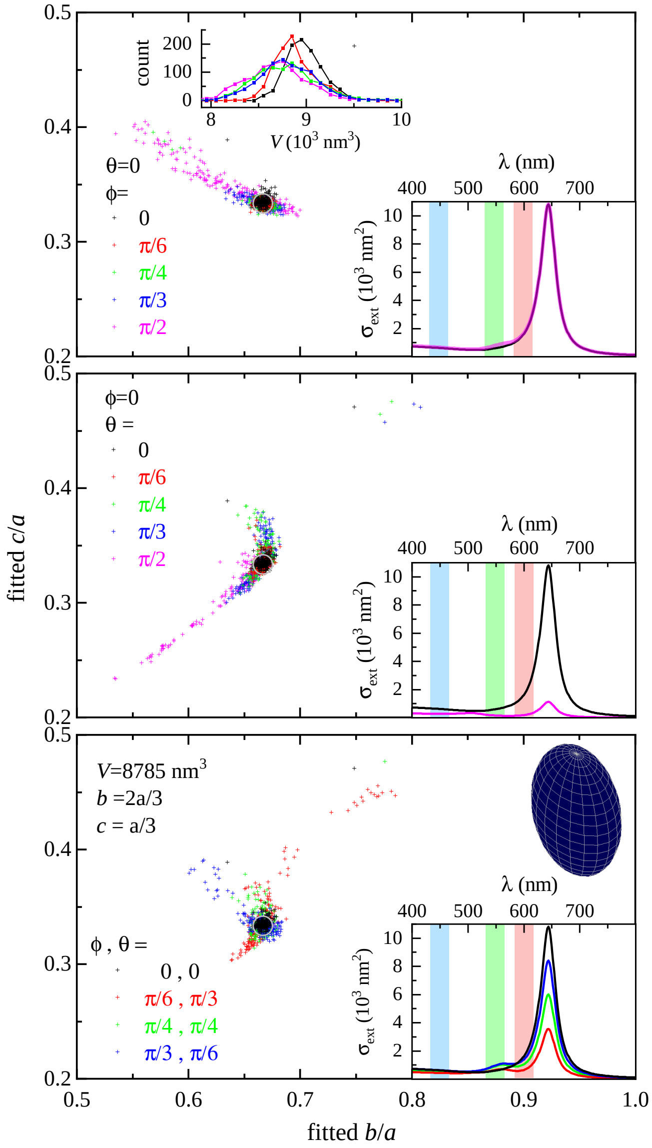

Figure S6. As Fig. 6, but for an ellipsoidal NP with $V = 8785\,\mathrm{nm}^3$, $b = 2a/3$, $c = a/3$, and for $\psi = 0$ and several ϕ and θ, as indicated.

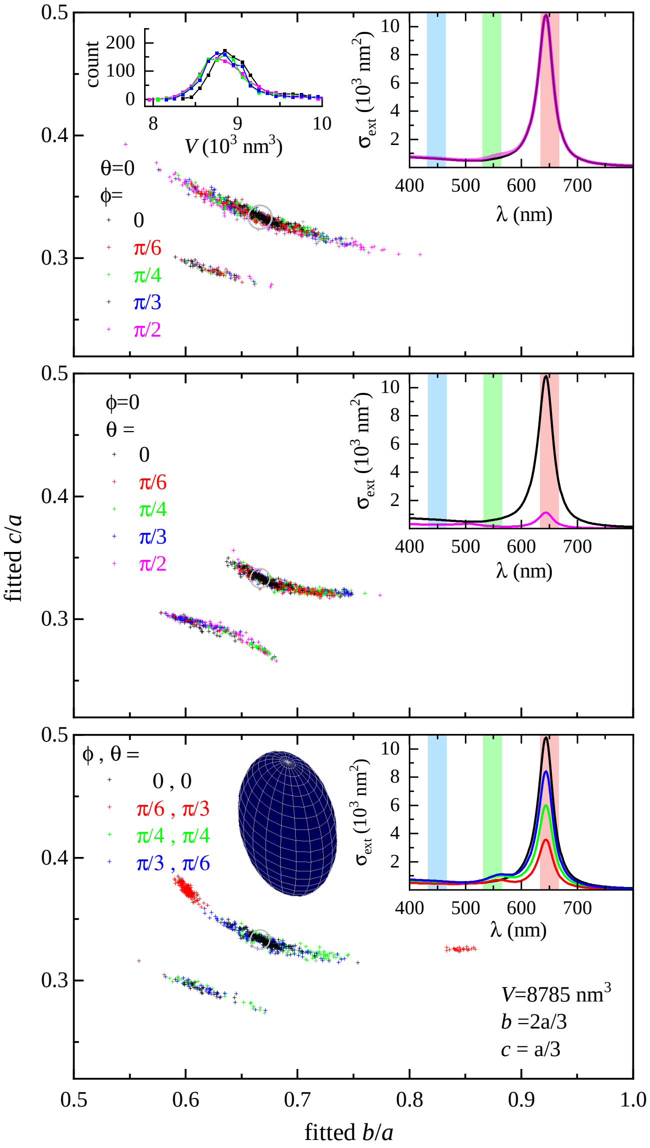

Figure S7. As Fig. S6, but for $\{\Lambda\} = \{450, 550, 650\}$.

clear general improvement in the accuracy of aspect ratios. However, the accuracy of the volume is improved across the different rotations explored.

D. Extinction-cross-sections of spherical gold NPs

Here we discuss the accuracy of the calculated extinction cross-sections of spherical gold NPs in the dipole approximation, which is used for the nanosizer fits throughout the present work. The accuracy is affected by two factors: the dipole approximation and the permittivity used to describe gold. Let us first discuss the dipole approximation, which is valid in the limit of small NPs. To investigate its accuracy, we compare in Fig. S8 the extinction cross-section in the dipole limit with full calculations using a finite element solver [S5]. In Fig. S8a, results are shown for different NP diameters, and we find that while for a diameter of 20 nm, the deviations are below 10%, they increase with size, providing a broadening and a red-shift. For a diameter of 30 nm, shown in Fig. S8b, we find a red-shift of about 6 nm, and a broadening of about 5 nm. The colour channels $\{\Lambda\} = \{450, 550, 600\}$ used in the 30 nm UGNSs measurements are shown as shaded areas. We find an increase of 20% for $\Lambda = 600$, 4% for $\Lambda = 550$, and a negligible change for $\Lambda = 450$.

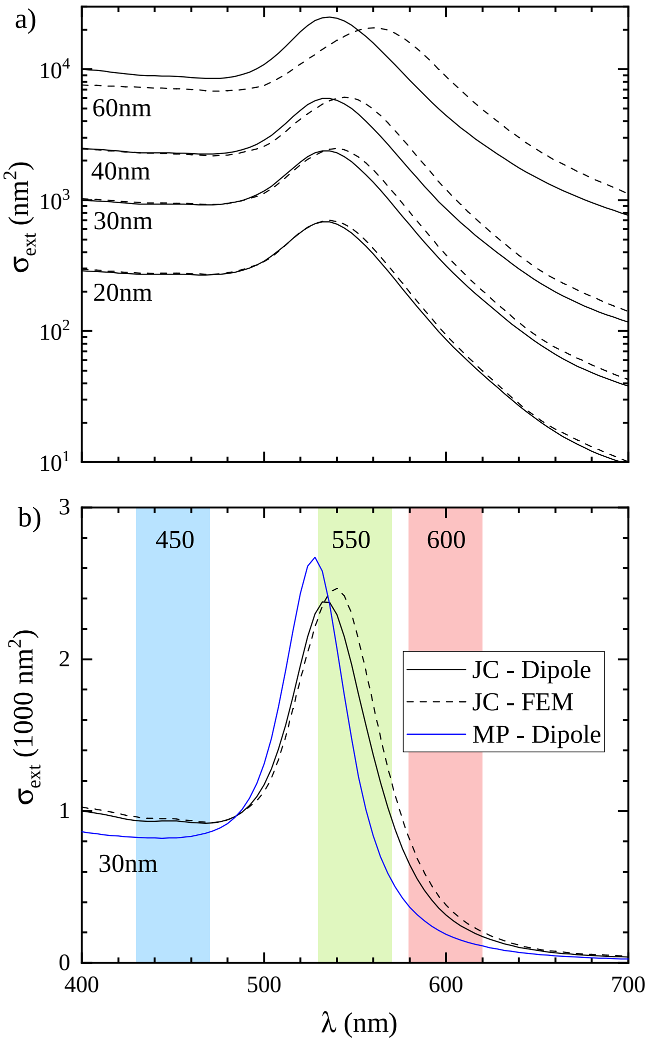

Figure S8. Calculated extinction cross-section spectra of a gold sphere in a medium of $n = 1.52$ refractive index. a) Using the dipole approximation (solid lines) or finite-element simulations (dashed lines), for different sphere diameters as labelled, and the permittivity data from Johnson & Cristy (JC) [S3]. b) as a), but only for 30 nm diameter, and additionally showing the dipole approximation using the permittivity data from McPeak et al. (MP) [S4]. The shaded areas indicate the colour channels used in the measurements of the UGNSs.

The second consideration is the accuracy of the permittivity used to describe gold. There are several data sets available [S5], which differ to some extent, and we used the one from Johnson & Cristy (JC) [S3]. Using instead the one from McPeak et al. [S4] in the dipole approximation (see the blue line in Fig. S8b), a blue-shift by some 5 nm, and a reduction of linewidth is observed. Furthermore, the cross-section for $\Lambda = 450$ is reduced by about 15%. We thus find that the variation between the different permittivity datasets is a relevant effect, of similar magnitude as the systematic error due to the dipole approximation for 30 nm diameter. Importantly, the bulk permittivity has been shown to need corrections when applied to NPs, and an additional surface scattering term has been added to the Drude model to account for an observed larger linewidth and redshift of small gold NPs [S6, S7]. Such a scattering term can also account for lattice defects inside the NPs. Furthermore, non-local response effects become relevant for very small NPs [S8].

Overall these uncertainties in the description will lead to systematic errors in the determination of the NP shape and size by the nanosizer. Notably, the dipole approximation can be left behind by using finite element modeling. For example, the implementation in Ref. S5 can be adapted to use the nanosizer to determine NP permittivities from their shape and measured cross-sections.

E. NP geometry determined by fits - 30 nm UGNSs

Here we discuss the influence of the choice of colour channels and gold permittivity dataset on the fitted NP size and shape for the UGNSs. In the main text we have shown i

In Fig. 7 of the main text, we have shown results using the two channels $\{\Lambda\} = \{450, 550\}$. Adding the $\Lambda = 600$ channel, the fit results are shown in Fig. S9. In view of the variability of the cross-section in the $\Lambda = 600$ channel due to both the choice of permittivity dataset and to the dipole approximation, as dicussed in Sec. S.II D, we can anticipate that the model underestimates the cross-section in this channel. In order to fit the measured data, the model introduces a NP asymmetry, as seen in Fig. S9 compared to Fig. 7.

To investigate this further, we fit the data using all possible selections of two out of the three available channels, as shown in Fig. S10. It is striking to observe that for $\{\Lambda\} = \{450, 600\}$, the NPs are fitted to be strongly oblate, with an aspect ratio c/a around 0.52, lying flat on the substrate ($\theta \approx 0$). Without the $\Lambda = 550$ channel, the model thus adjusts the aspect ratio to shift the LSPR to the red, to match the $\Lambda = 600$ cross-section, while at the same time keeping the in-plane asymmetry small to match the small polarizer angle dependence α. Notably, the fitted NP volume is reduced by this flattening for a given cross-section for in-plane polarization. This can be seen in Fig. 2b, where the cross-section at constant volume increases at 450 nm by about 50% for b/a going from 1 to 2.

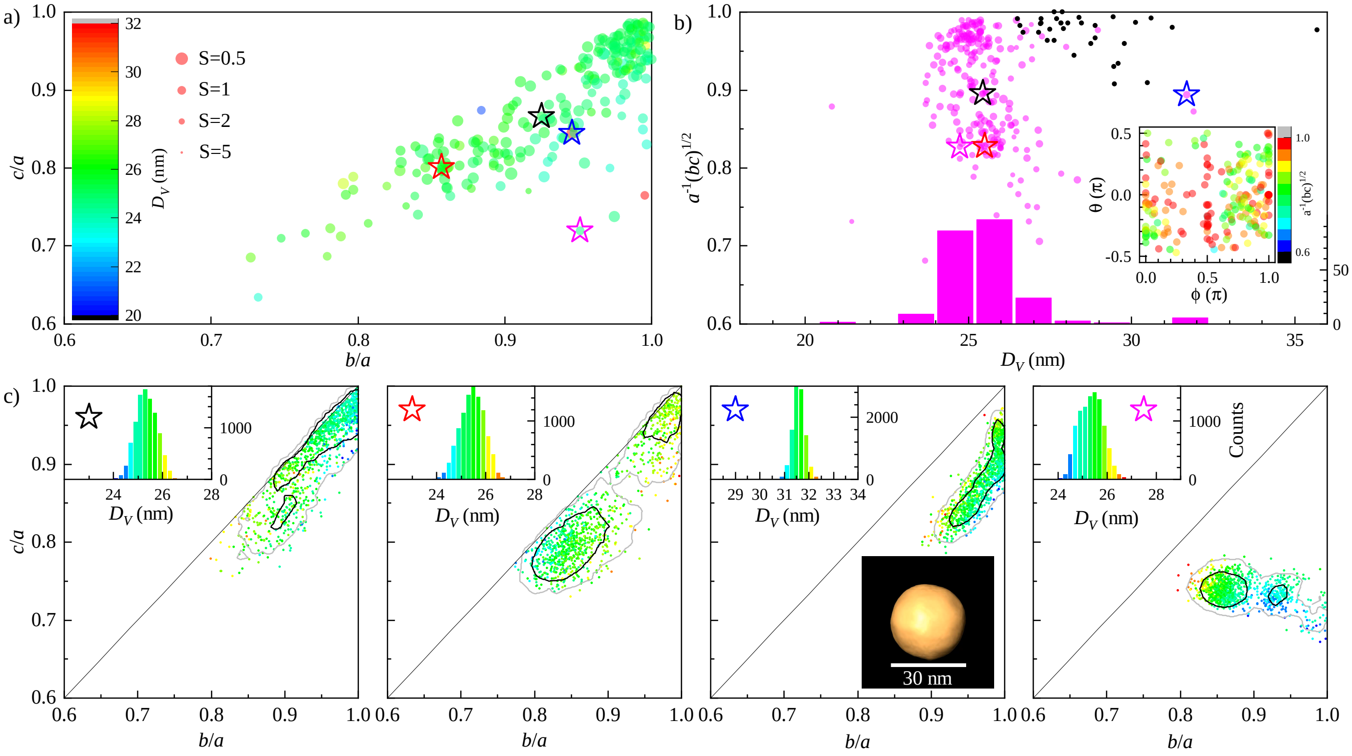

Figure S9. As Fig. 7, but for $\{\Lambda\} = \{450, 550, 600\}$.

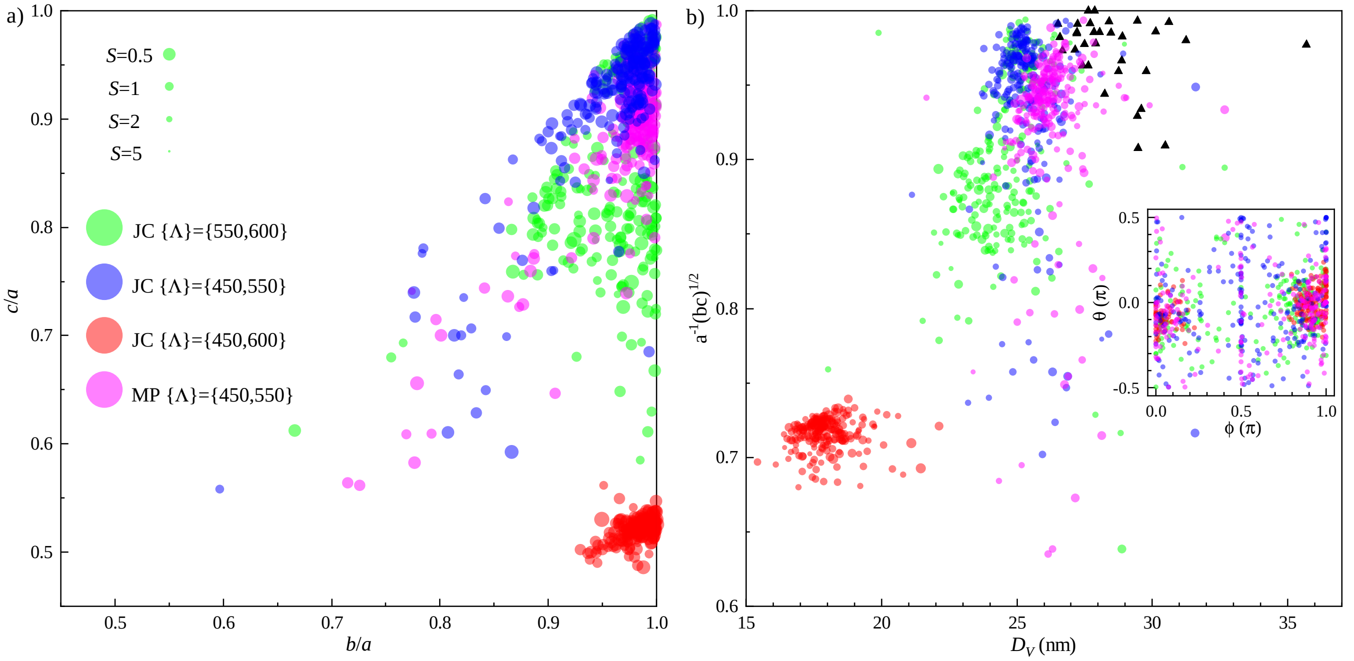

Figure S10. As Fig. 7 a) and b), but using different colour channels and permittivity data as indicated. Johnson & Cristy (JC) [S3] for $\{\Lambda\} = \{550, 600\}$, $\{\Lambda\} = \{450, 550\}$, and $\{\Lambda\} = \{450, 600\}$, as well as McPeak et al. (MP) [S4] for $\{\Lambda\} = \{450, 550\}$.

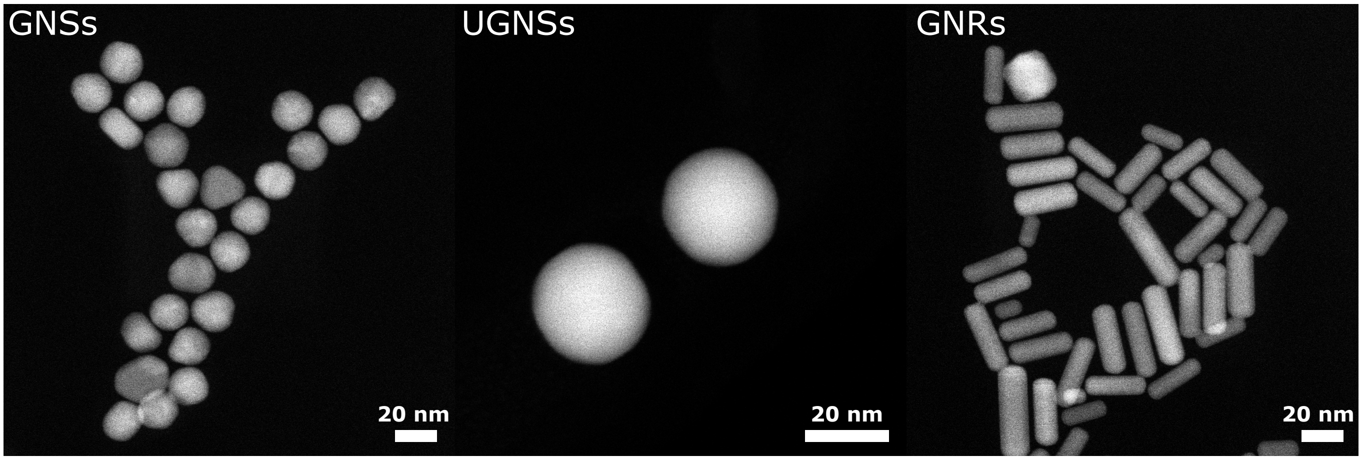

Figure S11. 2D projection HAADF-STEM images of the three NP samples.

Using instead $\{\Lambda\} = \{450, 550\}$, as used in the main text, the fitted shape is nearly spherical, with most NPs having aspect ratios around 0.95, consistent with the results of TEM. Clearly, in this case the model is not forced by the $\Lambda = 600$ channel to red-shift the LSPR, and the aspect ratios are instead determined by the measured polarizer angle dependencies only. Notably, the spherical shape also provides larger D_V, closer to the TEM data. A few NPs still show large asymmetries, consistent with the subset of asymmetric particles found in the polarization dependence, see Fig. 5a, and also represented by one NP at the bottom right of the TEM image shown in there.

Using $\{\Lambda\} = \{550, 600\}$, the fitted shape is between the two previous cases, still with the tendency to result in oblate particles, but with moderate aspect ratios of $c/a \approx 0.8$.

By changing the permittivity dataset from Johnson & Cristy (JC) [S3] to McPeak et al. [S4], instead of using different colour channels, we find a slightly larger D_V, and slightly oblate NPs. This can be understood looking at Fig. S8b, where the lower cross-section at 450 nm requires a larger volume, and the blueshift is compensated by making the NPs oblate.

We also note that the model assumes an ellipsoidal shape to apply the dipole approximation, and therefore does not cater for the effect of faceting of the NPs, which is however seen in the tomography of the 30 nm GNSs in Sec. S.III. Such faceting generally red-shifts the LSPR of near-spherical NPs [S9, S10], consistent with the underestimation of the cross-section in the $\Lambda = 600$ channel by the model.

NP type	$\bar{p}_{D\mathrm{v}} \pm \hat{p}_{D\mathrm{v}}$(nm)	$\bar{p}_{b/a} \pm \hat{p}_{b/a}$
UGNS	28.73 ± 1.81	0.973 ± 0.024
GNS round	19.31 ± 1.60	0.942 ± 0.047
GNS plates	20.63 ± 1.57	0.760 ± 0.129
GNR	16.03 ± 2.69	0.357 ± 0.068

Table S1. HAADF-STEM derived mean and standard deviation of parameters p_i. Here we consider the two main semi-axes seen in the 2D projection, and assign the longer to a, and the shorter to b and c.

S.III. HAADF-STEM

A. 2D projection images

2D projection images were taken from the three NP batches, with an example shown in Fig. S11. The images were analyzed to provide the visible 2D projection dimensions, in the same way as the TEM images shown in Fig. 5. The resulting distributions are given in Fig. S12 for the UGNSs, in Fig. S13 for the GNSs, and in Fig. S14 for the GNRs, together with the results of the nanosizer as in the corresponding figures in the main paper. The resulting distributions are broadly comparable with the TEM results, as also shown by the parameter distributions shown in Table S1. The GNSs were separated into roundish, triangular, and plate-shaped NPs, analyzed separately with the corresponding conversion from measured dimensions into the parameters.

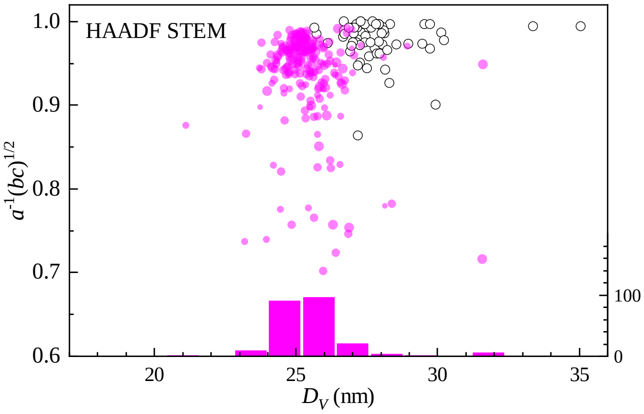

Figure S12. As Fig. 7b, but showing the results of HAADF-STEM. Black circles: b/a versus $D_V = 2\sqrt[3]{ab^2}$, for 61 NPs examined using HAADF-STEM. Magenta points: geometric average aspect ratio, $\sqrt{bc}/a$, versus D_V, determined by the optical nanosizer. The magenta bars give the histogram of the magenta points.

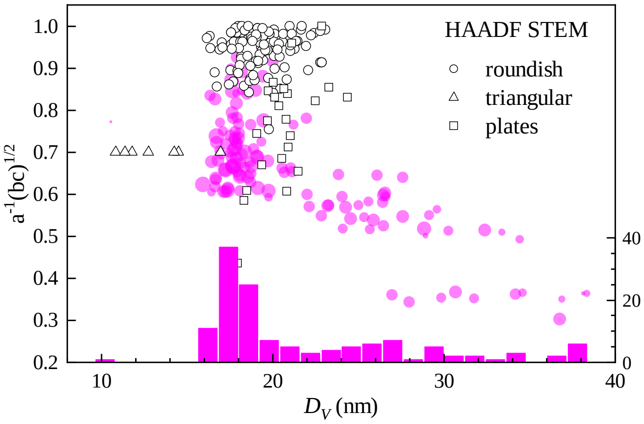

Figure S13. As Fig. 8b, but showing the results of HAADF-STEM. Black circles: for 104 roundish NPs, b/a versus $D_V = 2\sqrt[3]{ab^2}$. Black triangles: for 7 triangular NPs, $h/\sqrt{A}$, versus $D_V = \sqrt[3]{6Ah/\pi}$, where A is the measured triangle area, and h the height, assumed to be $0.7\sqrt{A}$ for illustration. Black squares: for 23 rod-shaped NPs, b/a versus $D_V = \sqrt[3]{12ab^2}$

B. Tomography

HAADF-STEM tomography was performed on two representative NPs from each sample batch as described in section 3.2 of the main text. For the 3D visualization, as presented in Fig. S15, isosurfaces were created using a manually determined grey value threshold and downsampled by a factor of 8 to smooth noise. The visualizations were performed in Amira 5.4.0. In Fig. S15 it can be observed that the UGNSs and GNRs display very uniform and faceted morphologies indicating that these NPs are defect-free. Indeed, the HAADF-STEM images in Fig. S11 confirm this observation. On the contrary, the GNSs exhibit many crystal defects resulting in more irregular shapes (Fig. S15).

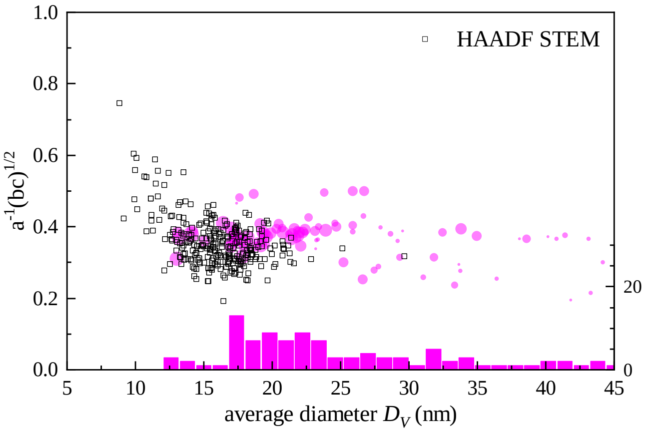

Figure S14. As Fig. 9b, but showing the results of HAADF-STEM. Black squares: for 297 rod-shaped NPs, b/a versus $D_V = \sqrt[3]{12ab^2}$

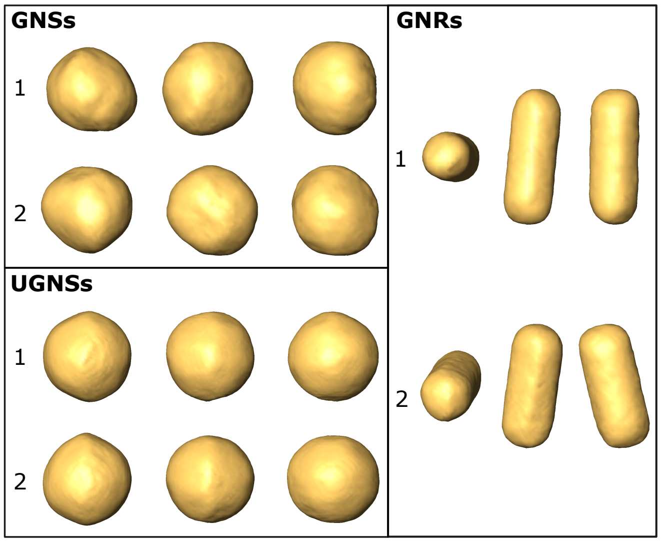

Figure S15. 3D visualization of the reconstructed tomography series for two NPs per sample. Snapshots along the same three different viewing directions (xy, xz and yz) are shown for each NP.

To determine the volume of the NPs, the reconstructions were segmented using Matlab 2019a using the same threshold value as for the visualizations. The aspect ratios were determined by measuring the width and length of the NP in an oblique slice through the middle of the NP. The obtained volumes and aspect ratios are summarised in Table S2. The obtained aspect ratios from the 3D reconstructions are compared to the ones obtained from the 2D projection along 0° tilt angle of the same NP as also shown in Table S2. In both cases the aspect ratios were determined using two orthogonal lines. Although the obtained aspect ratios are similar, slight differences occur. By using 2D projections, the aspect ratios of the GNSs and UGNSs seem to be slightly lower and the NPs appear more homogeneous. For the GNRs the opposite is observed and the aspect ratios are rather overestimated from the 2D projection images. However, it should be noted that the extracted values also depend on the exact measurement position, in 3D as well as 2D. This is especially true for the irregular GNSs, for which the lengths of a different set of orthogonal lines might result in slightly different aspect ratios for the same NP.

NP	Volume ($10^3\,\mathrm{nm}^3$)	AR from 3D	AR from 2D
GNS1	3.70	1.23	1.05
GNS2	3.38	1.11	1.02
UGNS1	13.10	1.01	1.02
UGNS2	12.10	1.04	1.00
GNR1	1.54	2.79	2.89
GNR2	3.58	2.39	2.45

Table S2. Measured NP volumes and aspect ratios (ARs) for the NPs from Fig. S15. A comparison is made between the measured ARs obtained from the 3D reconstruction and the corresponding 2D projection image of the same NP. The ARs were calculated by dividing the length of two orthogonal lines through the middle orthoslice (3D) or the projection image (2D).

[S1] C. Moler, *Makima Piecewise Cubic Interpolation* (2019), https://blogs.mathworks.com/cleve/2019/04/29/makima-piecewise-cubic-interpolation/.

[S2] C. Moler, *Splines and Pchips* (2012), https://blogs.mathworks.com/cleve/2012/07/16/splines-and-pchips/.

[S3] P. B. Johnson and R. W. Christy, Phys. Rev. B **6**, 4370 (1972).

[S4] K. M. McPeak, S. V. Jayanti, S. J. P. Kress, S. Meyer, S. Iotti, A. Rossinelli, and D. J. Norris, ACS Photon. **2**, 326 (2015).

[S5] A. Zilli, W. Langbein, and P. Borri, ACS Photonics **6**, 2149 (2019).

[S6] O. L. Muskens, P. Billaud, M. Broyer, N. Del Fatti, and F. Vallée, Phys. Rev. B **78**, 205410 (2008).

[S7] B. Foerster, A. Joplin, K. Kaefer, S. Celiksoy, S. Link, and C. Sönnichsen, ACS Nano **11**, 2886 (2017).

[S8] T. Christensen, W. Yan, A.-P. Jauho, M. Soljačić, and N. A. Mortensen, Phys. Rev. Lett. **118**, 157402 (2017).

[S9] X. Lin, S. Lin, Y. Liu, M. Gao, H. Zhao, B. Liu, W. Hasi, and L. Wang, Langmuir **34**, 6077 (2018).

[S10] J. Y. Bae, D.-W. Jung, C. B. Jeong, H.-S. Kim, J. D. Kim, H.-J. Ro, S. Jun, D. U. Kim, J. M. Kim, G.-R. Yi, G. Lee, and K. S. Chang, Particle & Particle Systems Characterization **36**, 1900131 (2019).